Electronic Supplementary Material (ESI) for Journal of Materials Chemistry A.

Supporting Information

A Data-Mining Approach to Understanding the Impact of Multi-doping on the Ionic Transport Mechanism of Solid Electrolytes Materials: The Case of dual-doped $Ga_{0.15}/Sc_y$-$Li_7La_3Zr_2O_{12}$

Henry A. Cortés[1], Mauricio R. Bonilla[1], Herbert Früchtl[2], Tanja van Mourik[2], Javier Carrasco[3,4], and Elena Akhmatskaya[1,4]

[1]BCAM - Basque Center for Applied Mathematics, Alameda de Mazarredo 14, E-48009 Bilbao, Spain
[2]EaStCHEM School of Chemistry, University of St Andrews, St Andrews, United Kingdom
[3]Centre for Cooperative Research on Alternative Energies (CIC energiGUNE), Basque Research and Technology Alliance (BRTA), Alava Technology Park, Albert Einstein 48, 01510, Vitoria-Gasteiz, Spain
[4]IKERBASQUE, Basque Foundation for Science, Plaza Euskadi 5, 48009 Bilbao, Spain

S1. Force-field database and validation.

S1.1 DFT Databse

The database of structures employed to adjust the Buckingham potential parameters (see Table 1 of the main text) is summarized in Table S1. The energies, stresses, and forces were extracted using density functional theory (DFT). All structures consist of 8 formula units (f.u.) of substituted LLZO. For a temperature $T = 0$ K, the structures were subjected to energy minimization at constant volume (i.e., ions were allowed to move while the cell parameters remained fixed). For $T > 0$ K, the structures were extracted from 2 ps long *ab initio* molecular dynamics (MD) simulations. $0\%T_d$ and $100\%T_d$ correspond to structures in which all Ga ions are located in octahedral (O_h) or tetrahedral (T_d) Li^+ sites, respectively.

Table S1: Number of structures employed to adjust the Buckingham potential for $Ga_{0.15}/Sc_y$-$Li_7La_3Zr_2O_{12}$.

LLZO 8 f.u.	T(K)	$100\%T_d$	$0\%T_d$	Total
$Li_{53}Ga_1La_{24}Zr_{15}O_{96}$	0	306	209	525
$Li_{53}Ga_1La_{24}Zr_{15}O_{96}$	900	500	500	1000
$Li_{53}Ga_1La_{24}Zr_{15}O_{96}$	1000	100	100	200
$Li_{54}Ga_1La_{24}Zr_{15}Sc_1O_{96}$	0	60	64	124
$Li_{54}Ga_1La_{24}Zr_{15}Sc_1O_{96}$	900	500	500	1000
$Li_{54}Ga_1La_{24}Zr_{15}Sc_1O_{96}$	1000	100	100	200
			Total	3049

S1.2 Force field validation

Figure 3 in the main text presents validation results for the lattice constant (a) and conductivity (σ) of dual doped-$Ga_{0.15}/Sc_y$ LLZO, which are compared with the experimental values reported by Buannic et al. [1]. In this section, we compare the estimated values of a and σ for Sc-free Ga_x-doped LLZO with those presented in several experimental works for a range of the Ga content, x (Figure S1).

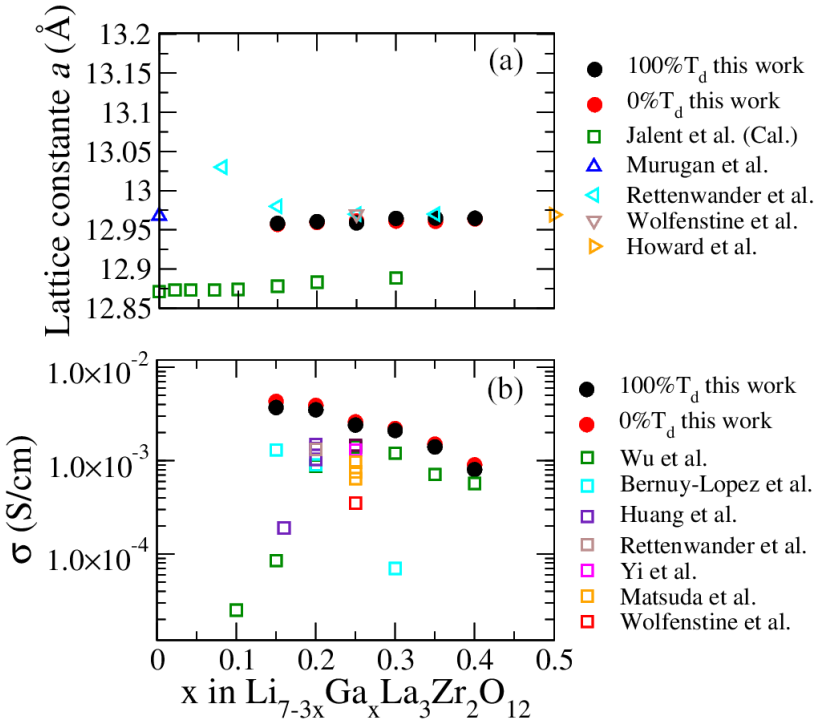

Figure S1: Computed (this work) and experimental lattice constant, a [2, 3, 4, 5, 6] (a) and ionic conductivity, σ [7, 8, 9, 10, 11, 12, 6] (b) of $Li_{x-3x}Ga_xLa_3Zr_2O_{12}$ at 300 K, as functions of the Ga content x.

S2. Ion clustering description.

The clustering process to classify the Li^+ ions according to the average displacement, $< d_i >$, is as follows:

a. Average Displacement Calculation:

For each Li^+ ion, we calculate the mean displacement $< d_i >$ across the simulation timeframe, t_{total}. $< d_i >$ is computed according to Eq. 2 in the main manuscript and is a weighted measure of the displacement that Li^+ ion i undergoes during the simulation run. To illustrate why not the "total displacement", $D_i = r_i(t_{total}) - r_i(0)$, was employed as a measure of mobility, see the schematic provided below:

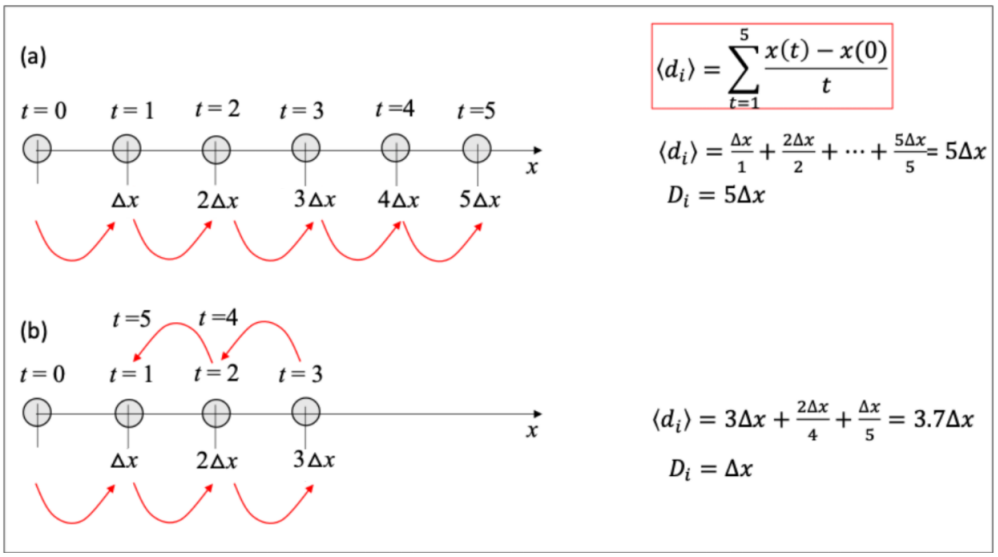

Figure S2: Average displacement ($< d_i >$) vs. Total displacement (D_i) - a schematic representation.

In both scenarios (a) and (b), a particle moves in one dimension and performs a jump of length Δx at each time step, for a total simulation time of 5. In (a), the particle moves monotonically away from its initial position. Thus, $< d_i >= D_i = 5\Delta x$, and i will be classified as a high mobility ion. In (b), the particle retraces its path at t = 4. Thus, $< d_i >= 3.7\Delta x$, while $D_i = \Delta x$. Whereas the total displacement would suggest that i is a low mobility ion, $< d_i >$ correctly indicates that i is actually a "middle" mobility ion that, due to stochasticity finished its trajectory at $t_{total} = 5$ close to the origin.

b. Clustering with k-Means:

The k-means algorithm is applied to the set of $\{< d_i >\}_{i=1,N}$ values, where N is the number of Li^+ ions. In k-means clustering, data points (in this case, $< d_i >$) are grouped into a specified number of clusters (k). The algorithm iteratively assigns each ion to one of the k clusters based on the closeness of its $< d_i >$ value to the cluster's mean (centroid). This process continues until the assignment of ions to clusters stabilizes (i.e., further iterations do not significantly change the composition of the clusters).

c. Elbow Method for Determining the Number of Clusters (k):

The elbow method was used to determine the optimal number of clusters ($k = 3$ in this case). It involves running the k-means clustering algorithm for a range of k values (1 to 9) and calculating the sum of squared distances from each point to its assigned center (also known as Within-Cluster-Sum-of-Squares). Then, it looks for the "Elbow Point" (see Figure S3), where the

rate of decrease changes sharply. This point is considered an indicator of the appropriate number of clusters.

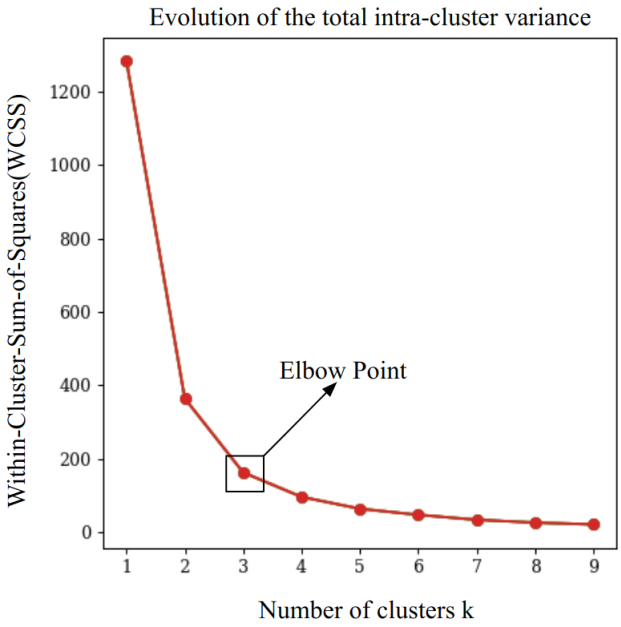

Figure S3: The evolution of the Within-Cluster-Sum-of-Squares (WCSS) versus the number of clusters k, with the 'Elbow Point' highlighted.

S3. Site analysis validation.

S3.1 Site identification and characterization

We have validated our DM-based site identification approach (Figure 2 of the main text) by analyzing undoped cubic LLZO with a 3×3×3 supercell. Figure S4 displays the cluster map associated with the Li-ion density. Each cluster corresponds to an individual Li^+ site, identified with a distinct color to facilitate visualization. The cluster map is entirely derived from MD trajectories without *a priori* knowledge of the system structure.

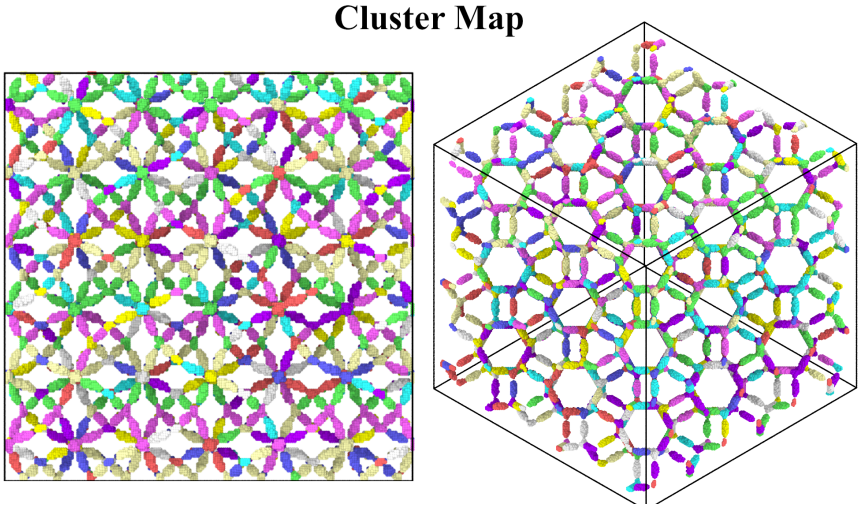

Figure S4: Cluster map of the undoped cubic LLZO 3×3×3 supercell in the (001) and (111) orientations.

The cluster map enables the calculation of site volumes (which are proportional to numbers of voxels in each cluster), site amplitude (which is a measure of the characteristic size of the site), the number of nearest neighbors (NN) for each site, and the site occupancy as follows:

- **Volume:** It is calculated by multiplying the number of voxels comprising the cluster by the size of each voxel. Notably, this particular calculation is also integral in establishing the density cutoff ρ_{cut} as described in the main text (see Figure 2 of main text).

- **Amplitude:** It is calculated by locating the cluster's centroid and subsequently measuring the distance from the centroid to the farthest voxel within the cluster.

- **Number of NN:** It is determined by counting the sites within a specified cutoff distance, d_{cut}, which is determined as

$$d_{cut} =< A_{site_1} > + < A_{site_2} > +(< A_{site_1} > + < A_{site_2} >) * 0.5, \quad (1)$$

where $< A_{site_1} >$ and $< A_{site_2} >$ are the average amplitudes of the two types of adjacent sites, and $(< A_{site_1} > + < A_{site_2} >) * 0.5$ is an extra term accounting for the interstitial space between them.

- **Occupancy:** It is determined by summing the density of all the voxels within the cluster, that is:

$$O_{site} = \sum_{i=1}^{c} \rho_i, \tag{2}$$

where O_{site} is the occupancy by site, c is the number of voxels forming the cluster, and ρ_i is the density in each voxel i.

Figure S5 (a) shows the number of voxels within each cluster. This data provides a clear differentiation between two types of sites, Type 0 and Type 1, denoted as black and red dots. Figures S5 (b) and (c) present the amplitudes and NN associated with the Type 0 and Type 1 sites.

In Figure S5 (a), we can observe the distribution of the number of voxels within each cluster, facilitating a clear distinction between two categories of sites: Type 0 and Type 1, represented by black and red dots, respectively. In Figures S5 (b) and (c), we delve deeper into the characteristics of these two site types, examining their amplitudes and number of NN.

Type 0 sites (black dots) exhibit an average amplitude of approximately 0.65 Å and are surrounded by 4 NN, aligning with the known characteristics of T_d sites [13]. In contrast, Type 1 sites (red dots) display an average site amplitude of around 1.1 Å and maintain 2 NN, in perfect agreement with the distinctive features attributed to O_h sites [13].

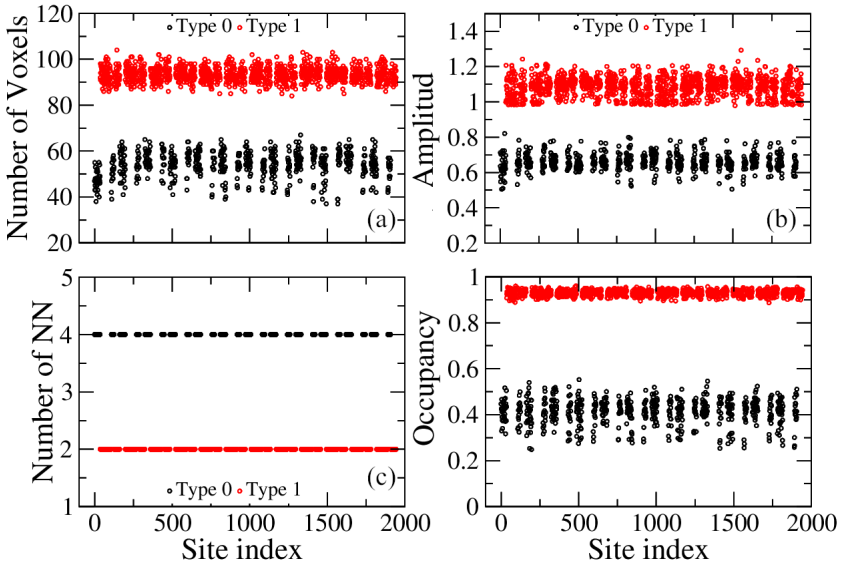

Figure S5: Site number of voxels (a), amplitude (b), number of nearest neighbors NN (c), and occupancy in cubic LLZO at 300K. Two types (Type 0 and Type 1) of sites are denoted by black and red dots, respectively.

Our methodology effectively allows us to identify the 1944 Li^+ sites of cubic LLZO within a 3×3×3 supercell, 648 24d T_d sites and 1296 48g/96h O_h sites. Moreover, the permissible range of Li-site occupancy falls within the limits of $0.333 \leq O_{T_d} \leq 0.55$ and $0.88 \leq O_{O_h} \leq 1.0$ [14]. These values align closely with those presented in Figure S5 (d) for Type 0 and Type 1 sites, respectively.

S3.2 Radial occupancy

The radial occupancy $rocc(r)$ between the sites Type 0 and Type 1 is defined as:

$$rocc_{0-1}(r) = \frac{1}{N_1^t} \sum_{i=1}^{N_0} \sum_{j=1}^{N_1} O_{ij}^1(r), \tag{3}$$

where $O_{ij}^1(r)$ is the occupancy of the sites Type 1 at a distance r within a spherical shell of thickness dr from sites Type 0, as illustrated in Figure S6. N_0 and N_1 are the number of sites of Type 0 and Type 1, respectively, and N_1^t is the total number of Type 1 sites considered (i.e., $N_1^t = \sum_{i=1}^{N_0} N_{1_i}$). In this work, we have extended r up to 10 Å using $dr = 0.5$ Å.

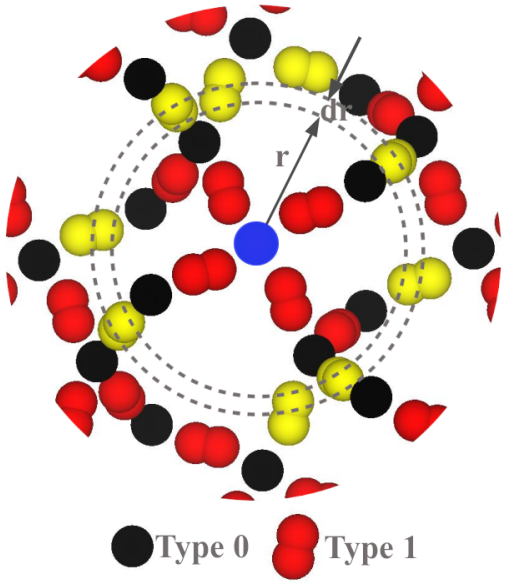

Figure S6: Schematic representation of radial occupancy, $rocc(r)$. Type 0 and Type 1 sites are represented by black and red spheres, respectively. Meanwhile, the blue and yellow spheres represent a specific site Type 0 and the sites at a distance r within a spherical shell of thickness dr from sites Type 0.

S4. $Ga_{0.15}/Sc_y$-LLZO conventional ionic conductivity.

Figure S7 illustrates the calculated ionic conductivity of $Ga_{0.15}/Sc_y$-LLZO at $T = 300$ with the conventional assumption that *all* Li-ions contribute equally to ionic conduction. Clearly, the behavior is somewhat erratic compared to that in Figure 3b of the main text, in which subdiffusive ions are not considered.

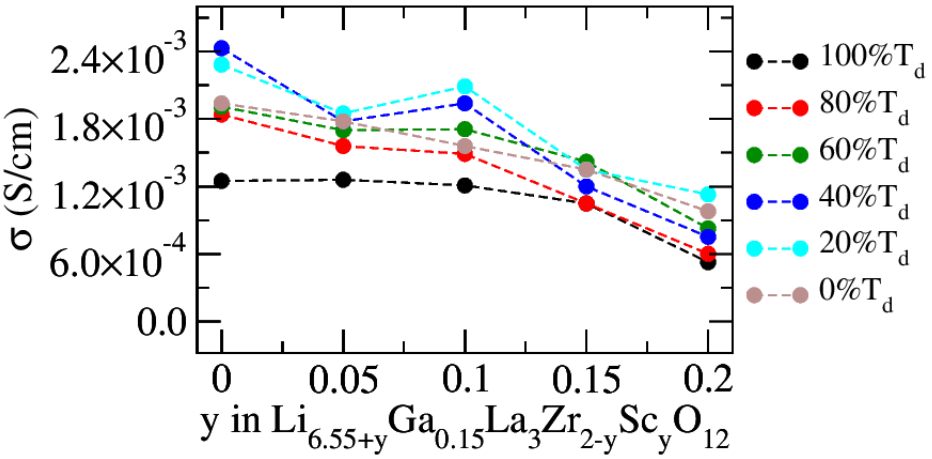

Figure S7: Calculated ionic conductivity, considering all Li ions as equals, of $Ga_{0.15}/Sc_y$-LLZO as a function of Sc^{3+} content (y) for several Ga^{3+} distributions ($\%T_d$) at T = 300 K.

S5. $Ga_{0.15}/Sc_y$-LLZO occupancy limits.

Let us consider a cubic $Li_7La_3Zr_2O_{12}$ unit cell (8 f.u.) with 56 Li^+ ions (N_{tot}) distributed across 72 Li^+ sites (i.e. 24 T_d and 48 O_h sites). We can define N_{T_d} and N_{O_h} as the numbers of Li^+ ions in T_d and O_h sites, respectively. Thus $N_{tot} = N_{T_d} + N_{O_h}$.

In the dual doped system $Li_{6.55+y}Ga_{0.15}La_3Zr_{2-y}Sc_yO_{12}$, if g Ga^{3+} and s Sc^{3+} ions are introduced in total, we have that

$$N_{T_d} + N_{O_h} = N_{tot} - 3g + s, \tag{4}$$

where each Ga^{3+} substitutes a Li^+ ion and produces 2 Li^+-vacancies, while a Sc^{3+} ion substitutes a Zr^{4+} ion and, therefore, introduces an additional Li^+ ion due to charge compensation.

In addition, a Ga^{3+} ion may occupy either a T_d or an O_h site. Thus, g can be split into two parts,

$$g = g_{T_d} + g_{O_h}. \tag{5}$$

Let us assume that all the T_d sites are initially occupied. Consequently, all O_h sites will be empty, as depicted in Figure S8 (a).

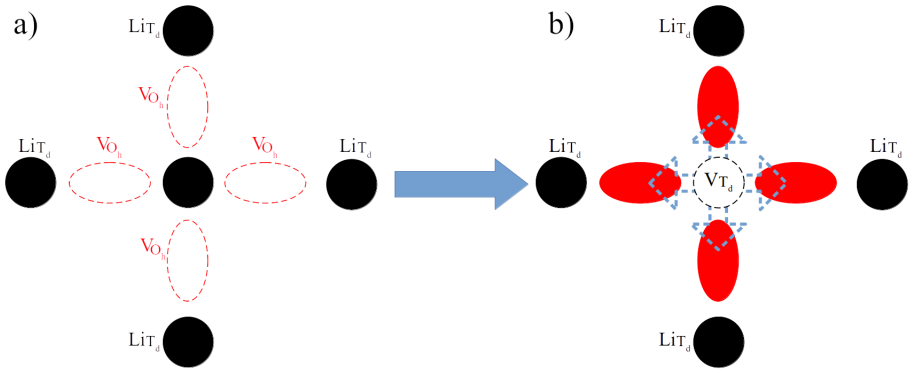

Figure S8: In these schematic representations, (a) illustrates a fully occupied T_d structure (full-black circles) with four adjacent empty O_h sites (empty-red ovals). (b) depicts the scenario where a Li^+ ion is removed from a T_d site (empty-black circle), leading to the occupation of adjacent O_h sites.

If we remove one Li^+ ion, then 4 Li^+ ions can now be put into the adjacent O_h sites. Thus, if x T_d sites are left empty, we get

$$N_{T_d} = 24 - g_{T_d} - x \tag{6}$$

and

$$N_{O_h} = 4x. \tag{7}$$

By plugging Eqs. (5), (6) and (7) in Eq. (4), we obtain

$$N_{T_d} = \frac{5}{9} - \frac{9}{18C}(f_{T_d} - \frac{3}{4}) - \frac{s}{72} \tag{8}$$

and

$$N_{O_h} = \frac{1}{36C}(32 - g(3 - f_{T_d})) - s, \tag{9}$$

where f_{T_d} is the fraction of Ga in T_d sites, defined as $f_{T_d} = (g - g_{O_h})/g$, and C is the number of unit cells in the structure.

Finally, the maximum and minimum limits for the occupation of the T_d and O_h sites is given by

$$O_{T_d} = \frac{N_{T_d}}{S_{T_d}} \tag{10}$$

and

$$O_{O_h} = \frac{N_{O_h}}{S_{O_h}}, \tag{11}$$

where S_{T_d} and S_{O_h} are the total numbers of sites of each type, respectively. In the case of a unit cell, those correspond to $S_{T_d} = 24$ for T_d and $S_{O_h} = 48$ for O_h.

S6. $Ga_{0.15}/Sc_{0.0}$-LLZO density maps.

Figure S9 shows the density maps of the Li subset Li_{hm} in the (100), (001), and (001) planes for the system $Ga_{0.15}/Sc_{0.0}$-LLZO in the $0\%T_d$ and $100\%T_d$ configurations (indicated above the plots) at 300 K.

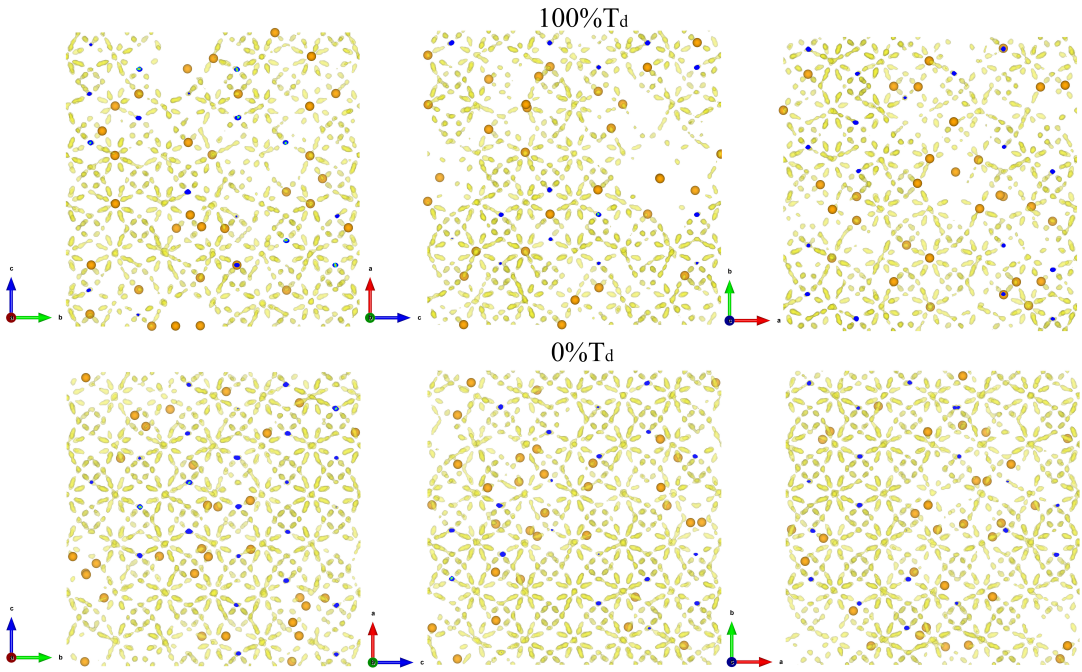

Figure S9: Density maps of Li_{hm} ions in the (100), (001), and (001) planes for $Ga_{0.15}/Sc_{0.0}$-LLZO with $0\%T_d$ (a) and $100\%T_d$ (b) at 300K. Ga^{3+} ions are represented as orange spheres.

References

[1] L. Buannic, B. Orayech, J.-M. López Del Amo, J. Carrasco, N. A. Katcho, F. Aguesse, W. Manalastas, W. Zhang, J. Kilner, and

A. Llordés, "Dual substitution strategy to enhance li$^+$ ionic conductivity in li$_7$la$_3$zr$_2$o$_{12}$ solid electrolyte," *Chemistry of Materials*, vol. 29, no. 4, pp. 1769–1778, 2017.

[2] R. Jalem, M. Rushton, W. Manalastas, M. Nakayama, T. Kasuga, J. A. Kilner, and R. W. Grimes, "Effects of gallium doping in garnet-type $Li_7La_3Zr_2O_{12}$ solid electrolytes," *Chem. Mater.*, vol. 27, no. 8, pp. 2821–2831, 2015.

[3] R. Murugan, V. Thangadurai, and W. Weppner, "Fast lithium ion conduction in garnet-type li$_7$la$_3$zr$_2$o$_{12}$," *Angewandte Chemie International Edition*, vol. 46, no. 41, pp. 7778–7781, 2007.

[4] M. A. Howard, O. Clemens, E. Kendrick, K. S. Knight, D. C. Apperley, P. A. Anderson, and P. R. Slater, "Effect of Ga incorporation on the structure and li ion conductivity of $La_3Zr_2Li_7O_{12}$," *Dalton Transactions*, vol. 41, pp. 12048–12053, 2012.

[5] D. Rettenwander, C. A. Geiger, M. Tribus, P. Tropper, and G. Amthauer, "A synthesis and crystal chemical study of the fast ion conductor $Li_{7-3x}Ga_xLa_3Zr_2O_{12}$ with $x = 0.08$ to 0.84," *Inorganic Chemistry*, vol. 53, no. 12, pp. 6264–6269, 2014.

[6] J. Wolfenstine, J. Ratchford, E. Rangasamy, J. Sakamoto, and J. L. Allen, "Synthesis and high li-ion conductivity of Ga-stabilized cubic $La_3Zr_2Li_7O_{12}$," *Materials Chemistry and Physics*, vol. 134, no. 2-3, pp. 571–575, 2012.

[7] J.-F. Wu, E.-Y. Chen, Y. Yu, L. Liu, Y. Wu, W. K. Pang, V. K. Peterson, and X. Guo, "Gallium-doped $Li_7La_3Zr_2O_{12}$ garnet-type electrolytes with high lithium-ion conductivity," *ACS Appl. Mater. Interfaces*, vol. 9, no. 2, pp. 1542–1552, 2017.

[8] C. Bernuy-López, W. Manalastas, J. M. López del Amo, A. Aguadero, F. Aguesse, and J. A. Kilner, "Atmosphere controlled processing of ga-substituted garnets for high li-ion conductivity ceramics," *Chemistry of Materials*, vol. 26, no. 12, pp. 3610–3617, 2014.

[9] X. Huang, J. Su, Z. Song, T. Xiu, J. Jin, M. E. Badding, and Z. Wen, "Synthesis of Ga-doped $Li_7La_3Zr_2O_{12}$ solid electrolyte with high Li^+ ion conductivity," *Ceramics International*, vol. 47, no. 2, pp. 2123–2130, 2021.

[10] D. Rettenwander, G. Redhammer, F. Preishuber-Pflugl, L. Cheng, L. Miara, R. Wagner, A. Welzl, E. Suard, M. M. Doeff, M. Wilkening, J. Fleig, and G. Amthauer, "Structural and electrochemical consequences of al and ga cosubstitution in li$_7$la$_3$zr$_2$o$_{12}$ solid electrolytes," *Chemistry of Materials*, vol. 28, no. 7, pp. 2384–2392, 2016.

[11] E. Yi, W. Wang, J. Kieffer, and R. Laine, "Key parameters governing the densification of cubic-li$_7$la$_3$zr$_2$o$_{12}$ li$^+$ conductors," *J. Power Sources*, vol. 352, pp. 156–164, 2017.

[12] Y. Matsuda, A. Sakaida, K. Sugimoto, D. Mori, Y. Takeda, O. Yamamoto, and N. Imanishi, "Sintering behavior and electrochemical properties of garnet-like lithium conductor $Li_{6.25}M_{0.25}La_3Zr_2O_{12}$ (M: Al^{3+} and Ga^{3+})," *Solid State Ionics*, vol. 311, pp. 69 – 74, 2017.

[13] C. Chen, Z. Lu, and F. Ciucci, "Data mining of molecular dynamics data reveals li diffusion characteristics in garnet $Li_7La_3Zr_2O_{12}$," *Sci Rep*, vol. 7, no. 1, p. 40769, 2017.

[14] S. Adams and R. P. Rao, "Ion transport and phase transition in li$_{7-x}$la$_3$zr$_{2-x}$m$_x$o$_{12}$ (m = ta^{5+}, nb^{5+}, x = 0, 0.25)," *Journal of Materials Chemistry*, vol. 22, pp. 1426–1434, 2012.